OPTICA

Electro-optic transduction in silicon via gigahertz-frequency nanomechanics

Han Zhao,[1,2] Alkim Bozkurt,[1,2] and Mohammad Mirhosseini[1,2,*]

[1]The Gordon and Betty Moore Laboratory of Engineering, California Institute of Technology, Pasadena, California 91125, USA
[2]Institute for Quantum Information and Matter, California Institute of Technology, Pasadena, California 91125, USA
*mohmir@caltech.com

Received 24 October 2022; revised 22 April 2023; accepted 23 May 2023; published 20 June 2023

Interfacing electronics with optical fiber networks is key to the long-distance transfer of classical and quantum information. Piezo-optomechanical transducers enable such interfaces by using gigahertz-frequency acoustic vibrations as mediators for converting microwave photons to optical photons via the combination of optomechanical and piezoelectric interactions. However, despite successful demonstrations, efficient quantum transduction remains out of reach due to the challenges associated with hybrid material integration and increased loss from piezoelectric materials when operating in the quantum regime. Here, we demonstrate an alternative approach in which we actuate 5-GHz phonons in a conventional silicon-on-insulator platform. In our experiment, microwave photons resonantly drive a phononic crystal oscillator via the electrostatic force realized in a charge-biased narrow-gap capacitor. The mechanical vibrations are subsequently transferred via a phonon waveguide to an optomechanical cavity, where they transform into optical photons in the sideband of a pump laser field. Operating at room temperature and atmospheric pressure, we measure a microwave-to-optical photon conversion efficiency of $1.72 \pm 0.14 \times 10^{-7}$ in a 3.3 MHz bandwidth. Our results mark a stepping stone towards quantum transduction with integrated devices made from crystalline silicon, which promise efficient high-bandwidth operation and integration with superconducting qubits. Additionally, the lack of need for piezoelectricity or other intrinsic nonlinearities makes our approach applicable to a wide range of materials for potential applications beyond quantum technologies.

https://doi.org/10.1364/OPTICA.479162

1. INTRODUCTION

Bidirectional conversion of electrical and optical signals is an integral part of telecommunications, and is anticipated to play a crucial role in long-distance quantum information transfer [1]. A direct electro-optic frequency conversion can be realized via the Pockels effect in nonlinear crystals [2–4]. More recently, the progress in controlling mechanical waves in nanostructures has led to a new form of effective electro-optic interaction, which is mediated via resonant mechanical vibrations [5]. In this approach, the electrical actuation of mechanical waves in piezoelectric materials is combined with the acousto-optic effect in cavity optomechanical systems to modulate the phase of an optical field. Piezo-optomechanical systems based on this concept have been used for microwave-optics frequency conversion [6–14] as well as optical modulation, gating, and nonreciprocal routing [15–17].

A variety of materials such as lithium niobate, gallium arsenide, gallium phosphide, and aluminum nitride have been previously used in piezo-optomechanical devices [6–14,18,19]. However, relying on a single material platform for simultaneously achieving strong piezoelectric and acousto-optic responses is challenging. Alternatively, heterogeneous integration has been used to combine piezoelectric materials with silicon optomechanical crystals (OMCs) [20–23]. These devices benefit from the large optomechanical coupling rates facilitated by the large refractive index and photo-elastic coefficient of silicon [24]. However, they require sophisticated fabrication processes, which hinder mass integration with the existing technologies. Additionally, heterogeneous integration often results in poly-crystalline films and degraded surface properties, which lead to increased microwave, acoustic, and optical loss when operating in the quantum regime [21].

Considering this landscape, a monolithic silicon platform for electro-optomechanical transduction is highly desirable. Beyond providing a large optomechanical coupling, silicon offers an exceptionally low acoustic loss in cryogenic temperatures [25–27], which facilitates efficient microwave-optical transduction. Previous work has pursued capacitive forces, as an alternative to piezoelectricity, for driving mechanical waves in silicon (which is not a piezoelectric due to its centro-symmetric crystalline structure) [28–30]. While efficient electro-optic transduction has been realized using this approach [31], the low frequency of the involved mechanical modes (1–10 MHz) has resulted in a small electro-optic conversion bandwidth. Conversely, large-bandwidth operation has been achieved by driving gigahertz-frequency acoustic waves [29], but achieving a large conversion efficiency has remained out of reach.

Here, we demonstrate electro-optomechanical transduction via a 5 GHz mechanical mode on a silicon-on-insulator platform. Our approach relies on a novel capacitive driving scheme for actuating mechanical vibrations in an extended geometry, where mechanical motion is shared between an electromechanical resonator and an optomechanical cavity via a phonon waveguide. By optimizing the design geometry, we maximize transduction efficiency in structures with robust performance against frequency disorder. We fabricate devices based on this concept and test them at room temperature and atmospheric pressure, where we achieve a microwave-optical photon conversion efficiency of $1.72 \pm 0.14 \times 10^{-7}$ in a 3.3 MHz bandwidth. Additionally, we employ the transducer devices as resonant phase modulators and quantify their performance by measuring a modulation half-wave voltage of 750 mV. Our platform's demonstrated efficiency and half-wave voltage are comparable to previous results in piezo-optomechanical devices. At the same time, our approach benefits from a significantly simplified fabrication process relying on conventional materials and techniques. Our work represents an essential first step towards developing piezoelectric-free silicon transducers for quantum transduction and may have implications for active RF photonics components, which are based on electrical actuation of mechanical waves in optomechanical devices [32–34].

2. PRINCIPLE OF OPERATION AND DEVICE DESIGN

Figure 1(a) depicts the chain of processes in our experiment, which consists of three main components: (i) coherent conversion of radio-frequency signals to mechanical waves, followed by (ii) routing and delivering of the acoustic wave to an OMC cavity, and (iii) creation of sideband optical photons by modulating the light inside the optomechanical cavity. We achieve the first component through electrostatic actuation, where a constant DC voltage across a mechanically compliant capacitor generates an electrostatic force of attraction. Modulating the voltage with a time-varying signal at the frequency ω creates an oscillatory component in the attraction force, $F(\omega) = (\mathrm{d}C/\mathrm{d}x)\, V_{\mathrm{dc}}\, V_{\mathrm{rf}}$, where $\mathrm{d}C/\mathrm{d}x$ is the rate of change of the capacitance with respect to the capacitor's gap x. This induced time-varying force resonantly drives a mechanical mode that is confined to the capacitor's electrodes.

The canonical setting for electro-optomechanical transduction couples a mechanical oscillator to a pair of microwave and optical cavities. In the electrostatically driven process under consideration, electromechanical interaction can be realized by connecting the DC-biased mechanically compliant capacitor to a microwave cavity. In this configuration, the electromechanical interaction rate (g_{em}) determines the electromechanical cooperativity [$C_{\mathrm{em}} = 4g_{\mathrm{em}}^2/(\gamma \cdot \kappa_{\mathrm{mic}})$, where γ and κ_{mic} are the intrinsic mechanical and microwave linewidths], which is a crucial figure of merit for calculating the transduction efficiency [1]. Alternatively, the capacitor can be directly attached to a microwave waveguide, as depicted in Fig. 1(a), without an intermediate microwave cavity. In this scenario, the electromechanical interaction leads to energy leakage via electromagnetic radiation into the waveguide. The rate of energy loss, known as the electromechanical decay rate (γ_{em}), is related to the cooperativity ($C_{\mathrm{em}} = \gamma_{\mathrm{em}}/\gamma$). While this direct connection to the waveguide typically yields lower cooperativies, it simplifies room-temperature experiments by not requiring a high-quality-factor microwave cavity (see Supplement 1 for more details).

While electrostatic actuation is the standard operation scheme for micro-electromechanical systems (MEMS) [35], its application to microwave-optical frequency conversion has remained relatively limited [28,29,36]. This is partly due to the difficulty in simultaneously achieving a large electromechanical conversion efficiency and confining high-Q mechanical resonances in the gigahertz-frequency band. Additionally, routing acoustic waves between the electromechanical and optomechanical systems is challenging due to the often dissimilar form factors of the mechanical vibrations employed in these distinct processes. We have recently solved some of these challenges in developing gigahertz-frequency *electromechanical crystals* (EMCs) and demonstrated operation in the strong coupling regime with large mechanical quality factors (approximately 10 million) in cryogenic environments [37]. EMC resonators rely on phononic crystal structures, and here we show that they can be engineered to interface with OMCs for realizing efficient microwave-optics transduction.

Figure 1(b) outlines the main components of our devices. A suspended silicon nanobeam with an array of air holes contains the electromechanical and optomechanical components, which are accessed via on-chip microwave and optical waveguides. The nanobeam starts with a phononic crystal "defect" cavity covered by a thin metallic layer that supports a "breathing" mechanical mode. Combined with a pair of electrodes that are symmetrically positioned across narrow air gaps, this section forms the EMC resonator [37]. The EMC section is adiabatically tapered to a phonon waveguide, which connects to an OMC cavity (based on the design in [24]) at the opposite end. The phonon waveguide

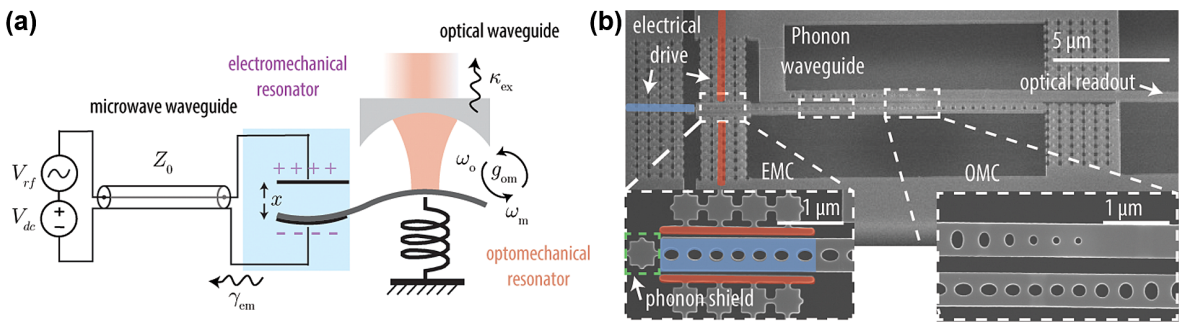

Fig. 1. Electro-optomechanical frequency conversion via electrostatic drive. (a) Schematic of the frequency conversion process. (b) Scanning electron microscope image of a fabricated device. The insets show the zoomed-in images of the optomechanical (OMC) and electromechanical crystal (EMC) resonators, respectively. Partial segments of the metalized "wire" connections and the EMC electrodes are shown in false colors (red and blue, for the two different polarities).

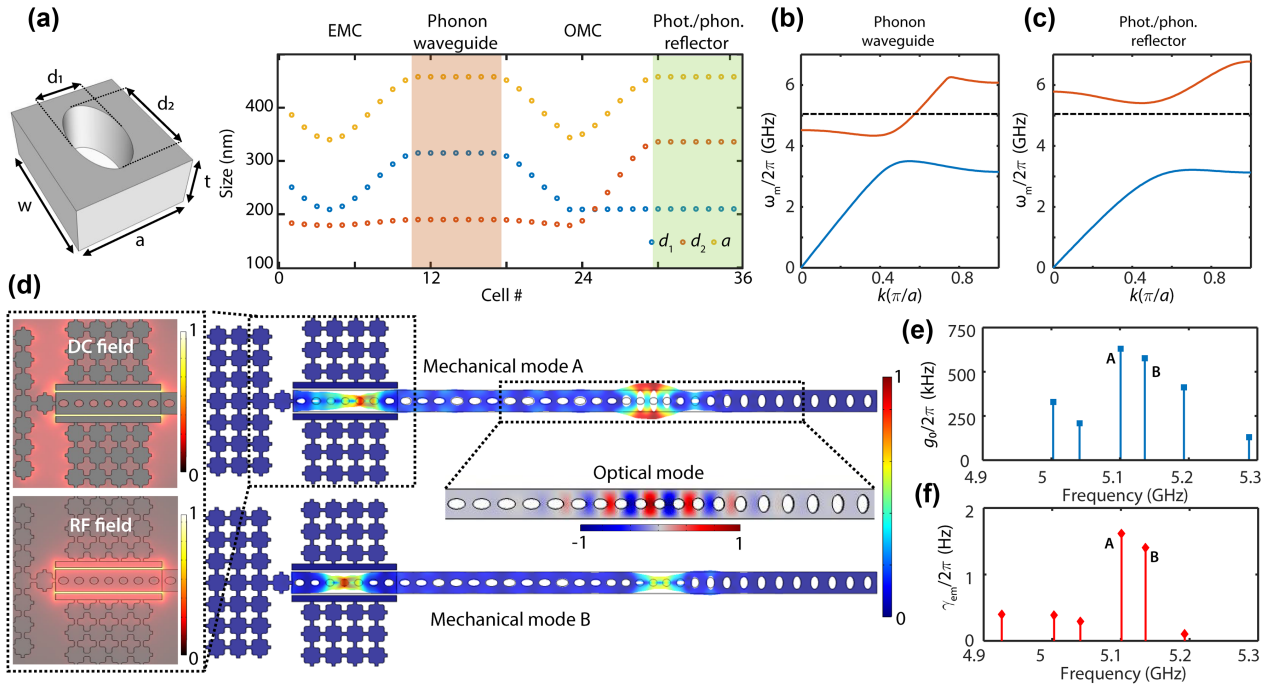

Fig. 2. Device design and modeling. (a) Geometric parameters of the nanobeam's elliptical hole array. The beam width $w = 530$ nm and thickness $t = 220$ nm are maintained throughout the structure. (b) Mechanical band structures of the phonon waveguide and (c) photon/phonon reflector used to terminate the OMC section. Dashed line marks the nominal frequency of the EMC and OMC resonators. (d) Simulated displacement field amplitudes for the two of the hybridized modes with the largest electro- and optomechanical couplings. The insets show the mode profile of the optical cavity field and the electric fields from the DC bias voltage and the microwave drive. A nonlinear color map is used to highlight the spatial distribution of the electric fields in the EMC. (e) Calculated optomechanical coupling rate of the simulated modes. (f) Electromechanical dissipation rate of the simulated modes, assuming a bias DC voltage of 10 V. The two dominant peaks correspond to the two hybridized modes in (d).

is designed to be reflective for the TE-polarized optical fields, but transmissive to the mechanical breathing mode of interest. Finally, the OMC cavity is terminated by a photon/phonon mirror section, which prevents optical and mechanical leakage into the membrane. The geometric parameters of the elliptical hole array defining the different sections of the nanobeam are displayed in Fig. 2(a). Additionally, we connect the nanobeam to the surrounding membrane via an array of two-dimensional phononic shields with a wide band gap for all phonon polarizations at the vicinity of the operation frequency (see Supplement 1).

We employ finite-element-method (FEM) simulations to model optical, electrical, and mechanical responses of the device [see Figs. 2(b)–2(f)]. As is evident in Fig. 2(d), the termination of the phonon waveguide with the EMC and OMC resonators creates a mechanical Fabry–Perot cavity, which supports extended "supermodes." The degree of overlap between the mechanical energy density of each supermode and the electric (optical) fields in EMC (OMC) resonators sets the rates of electromechanical (optomechanical) interactions. We numerically calculate the single-photon optomechanical coupling (g_0) and the electromechanical decay rate (γ_{em}) for all the supermodes in the vicinity of the bare resonance frequency of the EMC and OMC resonators. As is evident in Figs. 2(e) and 2(f), with careful design of the structure, we can get a pair of dominant supermodes in the spectra, which are identified as symmetric and anti-symmetric superpositions of the bare EMC and OMC resonances. We have numerically studied the effects of fabrication disorder on the degree of hybridization of the supermodes and optimized our design to achieve robustness against percent-level frequency offsets between the EMC and OMC resonators (see Supplement 1).

For each supermode, we have calculated the moving-boundary and photoelastic contributions to the optomechanical coupling via surface and volume integrals, respectively [24,27]. As previously mentioned, when our device is directly connected to a microwave waveguide, the electromechanical interaction is observed as a decay rate for the mechanical resonator. This decay rate can be understood as ohmic dissipation (modeling electromagnetic radiation through the waveguide) imparted by the electrical circuit onto the mechanical resonator. Considering the quadratical scaling of this decay rate via the biasing voltage, $\gamma_{em}(V_b) = V_b^2 \tilde{\gamma}_{em}$, we evaluate the per-volt electromechanical dissipation rate, $\tilde{\gamma}_{em}$, from device modeling. This is done by evaluating a normalized surface integral at the silicon/air boundaries in the device

$$\tilde{\gamma}_{em} = \frac{Z_0}{m_{eff} V_{dc}^2 V_{rf}^2}\left[\int\int_S (Q\cdot\hat{\boldsymbol{n}})\Delta\epsilon^{-1} D_{dc}^{\perp} D_{rf}^{\perp} dS\right]^2. \quad (1)$$

Here, $\Delta\epsilon^{-1} = 1/\epsilon_1 - 1/\epsilon_2$ represents the permittivity contrast between the two materials across the boundary; $D_{dc}^{\perp}$ and $D_{rf}^{\perp}$ are the normal components (to the structural boundary) of the DC and microwave electric displacement fields, respectively; m_{eff} is the frequency and the effective mass of the mechanical mode; and $Z_0 = 50\Omega$ is the impedance of the microwave feed line. We have normalized the displacement field, Q, such that $\max(|Q|) = 1$. The quantities V_{dc}, V_{rf} denote the voltage difference across the capacitor electrodes, expressed as line integrals of the corresponding electric fields. The distinction between the spatial profiles of the DC and RF electric fields is due to the frequency-dependent

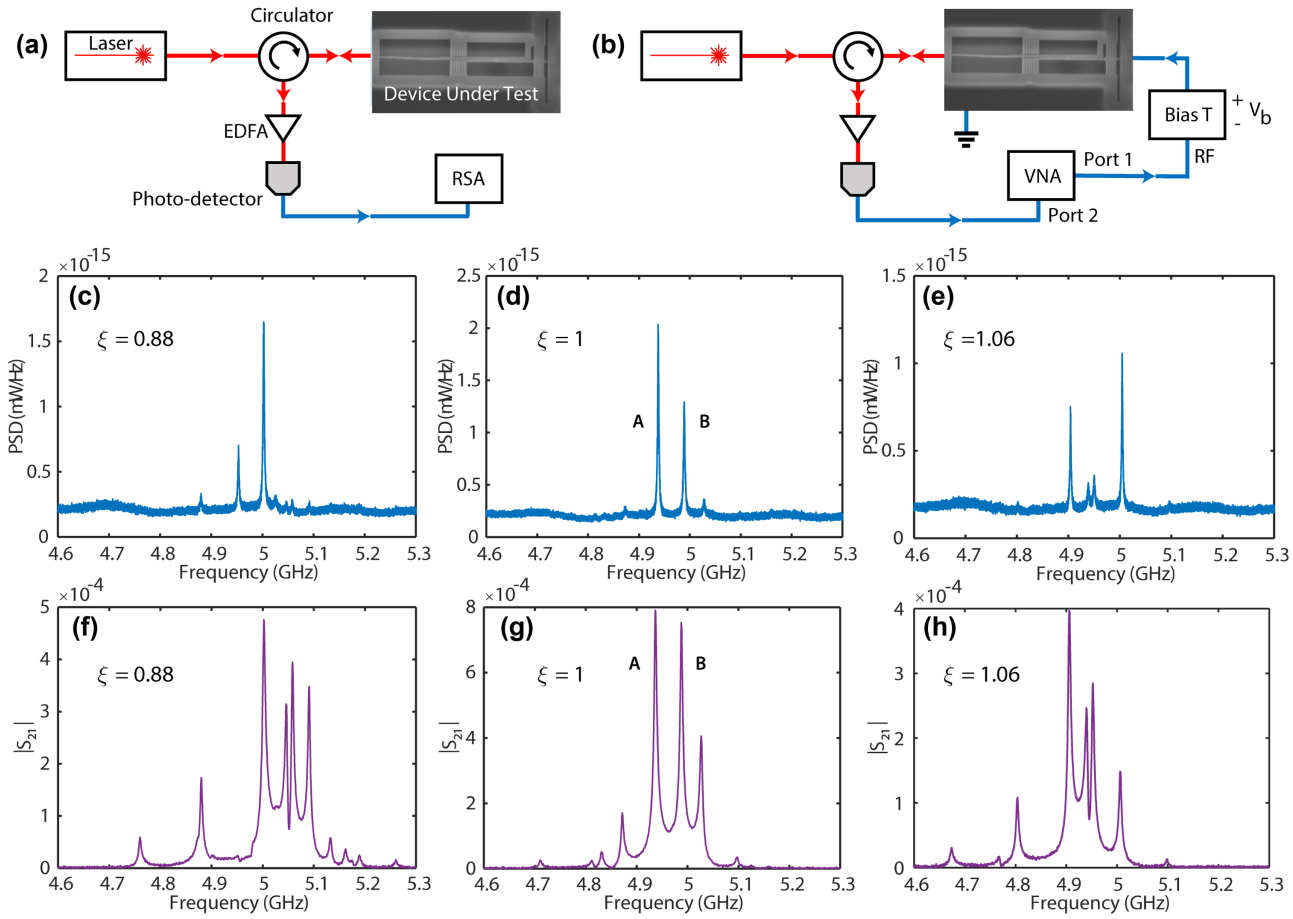

Fig. 3. Characterization of the optomechanical and electromechanical response. (a) Measurement setup for optomechanical detection of thermal mechanical motion. EDFA, erbium-doped fiber amplifier; RSA, real-time spectrum analyzer. (b) Measurement setup for microwave-to-optical frequency conversion. VNA, vector network analyzer. (c), (d), (e) Measurements of the optically transduced thermal mechanical spectrum for three devices with different values of the scale parameter, ξ. The measurements are performed with the pump laser detuned by $\Delta/2\pi \approx -5$ GHz from the optical cavity (blue sideband), and a laser power of 46 μW ($n_c = 980$) at the on-chip waveguide. (f), (g), (h) Corresponding microwave-to-optical transduction spectra for (c), (d), and (e). The DC bias is set to $V_b = 10$ V for the experiments in (c)–(e).

electric response of the substrate [see Fig. 2(d) and Supplement 1 for more details].

3. FABRICATION AND CHARACTERIZATION

We fabricate devices starting with a 220-nm silicon-on-insulator substrate sputtered with a thin ($t = 15$ nm) film of titanium nitride (TiN), which is used as the metallic layer for the electrodes. First, we pattern the nanobeam, phonon shields, and the optical waveguide by patterning the geometry via electron-beam lithography (EBL), followed by the dry etching through the metal and silicon layers via SF_6/Ar and SF_6/C_4F_8 chemistry, respectively. This step is followed by a second aligned EBL and etching processes to remove the metal layer from the optical components and define the electrodes. The devices are finally released with hydrofluoric (HF) acid.

Simplified diagrams of our measurement setups are presented in Figs. 3(a) and 3(b) (see more details in Supplement 1). We deliver the laser light to the chip by a tapered fiber waveguide [38], which is also used to collect the device's response in reflection. We characterize the optomechanical response by setting the laser frequency detuning from the optical cavity to one mechanical frequency ($\Delta = -\omega_m$, the "blue" side drive). In these initial measurements, we do not use any electric drive. Instead, the thermally excited mechanical motion from the ambient room-temperature environment leads to the conversion of power from the incident pump frequency into the optical resonance due to the optomechanical coupling. The generated sideband interferes with the reflected pump, leading to a beat note oscillating at the mechanical frequency. This beat note is measured with a fast detector and analyzed (on a spectrum analyzer) to find the spectrum of the thermally excited mechanical modes. Figures 3(c)–3(e) show the measurement results for three different devices. The presence of multiple peaks in the spectra points to the presence of hybridized supermodes. The areas under the peaks in the spectrum provide a relative measure of the optomechanical coupling rate (g_0) of the different modes (with a quadratic proportionality in the weak coupling regime, where $g_0 \ll \kappa$ for an optical linewidth of κ).

In the next step, we create electromechanical coupling by applying a DC voltage ($V_b = 10$ V) to the electrical port in the device. We then use a vector network analyzer (VNA) to excite the mechanical modes via a microwave drive as we measure the beat note in the photocurrent [Fig. 3(b)]. Figures 3(f)–3(h) shows the measurement results, where we can identify the mechanical supermodes with significant transduction efficiency. To achieve an

optimal mechanical spectrum, we precisely match the frequency of the electromechanical and optomechanical sections of the device. This is done post-fabrication, where we select the device with the optimal geometry from an array of devices with varying scale factors that create a mechanical frequency offset between the optomechanical and electromechanical components. The scale factor, denoted as ξ, is used to adjust the lattice constant ($a \to \xi a$) and the dimensions of the ellipse hole at the center of the electromechanical resonator ($d_1 \to \xi d_1$ and $d_2 \to \xi d_2$). We maintain the adiabatic tapering curve, phonon waveguide, and OMC parameters, as described in Supplement 1. We then determine the optimal device by searching for simultaneous maxima in the optomechanical and microwave-optics transduction spectra. In devices that are scaled close to optimally, we observe a pair of peaks in the transmission spectrum, which correspond to modes A and B [shown in Figs. 3(d) and 3(g)]. These findings are in agreement with our device modeling results [as shown in Figs. 2(e) and 2(f)]. Although the spectrum's fine features change, we find that all devices exhibit relatively strong transduction signals over a range of scaling parameter values. The peak transduction efficiency is maximized at $\xi = 1$, and drops to a quarter of its maximum value at $\xi = 1.06$, indicating that the devices are robust against small fabrication offsets.

We characterize the optomechanical and electromechanical coupling rates in a device with near-optimal geometry. Due to the small magnitude of the electromechanical decay rates, exclusive electrical measurement of the mechanical modes (e.g., via the reflection spectrum) is not possible in our experiment. Instead, we find the electromechanical decay rate by measuring the number of electrically excited phonons from a resonant drive with a known input power

$$n_{\mathrm{phon}} = \frac{\gamma_{\mathrm{em}}}{(\gamma/2)^2} \cdot \frac{P_{\mathrm{rf}}}{\hbar\omega_{\mathrm{m}}}. \tag{2}$$

Here, γ and ω_{m} are the (total) linewidth and the frequency of the mechanical oscillator, respectively, and P_{rf} is the power of the drive tone. We calibrate the number of phonons in the cavity by measuring the optically transduced power spectral density (PSD), which includes a narrow-band coherent response from the resonant drive along with an incoherent component from the thermal motion of the mechanical resonator [see Figs. 4(a) and 4(b)]. We find the driven phonon number by comparing these via

$$n_{\mathrm{phon}} = \frac{1}{e^{\frac{\hbar\omega_{\mathrm{m}}}{k_{\mathrm{B}}T}} - 1} \frac{S_{\mathrm{coh}}}{S_{\mathrm{th}}}, \tag{3}$$

where k_{B} is the Boltzmann constant, T is room temperature, and S_{coh} and S_{th} are the integrals of the coherent and thermal portions of the PSD, respectively. Using this technique, we find the electromechanical dissipation rates for the most prominent mechanical modes as $\gamma_{\mathrm{em}}^{\mathrm{A}}/2\pi = 0.85$ Hz and $\gamma_{\mathrm{em}}^{\mathrm{B}}/2\pi = 1.1$ Hz at $V_{\mathrm{b}} = 10$ V [see Figs. 4(a) and 4(b)]. We then calculate the optomechanical coupling for these two modes by measuring the change in the mechanical linewidth caused by the optomechanical back-action, $\Delta\gamma_{\mathrm{m}} = -4g_0^2 n_{\mathrm{c}}/\kappa$, as a function of photon number from the optical pump, n_{c}. Figure 4(c) shows measurement results, from which we calculate $g_0^{\mathrm{A}}/2\pi = 577 \pm 19$ kHz and $g_0^{\mathrm{B}}/2\pi = 470 \pm 24$ kHz using the measured value of the optical linewidth $\kappa/2\pi = 1.39$ GHz.

Using the measured electrical and optical coupling rates, we calculate the (internal) microwave-to-optical frequency conversion efficiency with the expression $\eta_{\mathrm{oe}} = 4\mathcal{C}_{\mathrm{em}}\mathcal{C}_{\mathrm{om}}/(1 + \mathcal{C}_{\mathrm{em}} + \mathcal{C}_{\mathrm{om}})^2$. Here, $\mathcal{C}_{\mathrm{em}} = \gamma_{\mathrm{em}}/\gamma$ and $\mathcal{C}_{\mathrm{om}} = 4g_0^2/\kappa\gamma$ are electromechanical and optomechanical cooperativities [1]. The measured efficiency [see Fig. 4(d)] is found to increase with the DC-bias voltage in a quadratic fashion, in accordance with the theoretical prediction. We find a maximum value of $\eta_{\mathrm{oe}} = 1.72 \pm 0.14 \times 10^{-7}$ for the mechanical mode A at $V_{\mathrm{b}} = 10$ V. The transduction bandwidth for this mode is measured as $B = 3.3$ MHz, which is set primarily by the intrinsic mechanical linewidth.

We crosscheck our measurement results by performing an alternative calibration of the electromechanical decay rate via direct observation of the optomechanical phase modulation. In analogy to the electro-optic modulators, we define the modulation index as $\beta \equiv 2g_0\sqrt{n_{\mathrm{phon}}}/\omega_m$. We are able to increase the modulation index by increasing the input microwave drive, which ultimately results in the generation of higher-order harmonics of the microwave drive tone in the optical emission from the cavity. These harmonics lead to the splitting of the optical reflection spectrum as the laser frequency sweeps near the optical resonance [see Fig. 4(e) and Supplement 1]. Fitting the reflection spectrum to a theory model, we can back out the modulation index. Subsequently, the efficiency of the modulator can be quantified by finding the half-wave voltage (V_π) that renders $\beta = \pi$. We can further relate V_π to the electromechanical decay rate via the expression

$$V_\pi = \frac{\pi\gamma\omega_{\mathrm{m}}}{4g_0}\sqrt{\frac{2Z_0\hbar\omega_{\mathrm{m}}}{\gamma_{\mathrm{em}}}}. \tag{4}$$

Using this technique, we find $\gamma_{\mathrm{em}}^{\mathrm{A}}/2\pi = 0.79 \pm 0.5$ Hz at $V_{\mathrm{b}} = 10$ V, in good agreement with the result from thermal motion calibration. We note that for the device under study we can reach values as small as $V_\pi = 750 \pm 12$ mV at $V_{\mathrm{b}} = 14$ V. This half-wave voltage is on par with previous realizations based on piezoelectric materials [6,13,19,22]. While in our current devices, the maximum DC-bias voltage is limited to $V_{\mathrm{b}} \approx 15$ V (limited by the onset of the pull-in instability; see Supplement 1), we anticipate further lowering of V_π to be possible in optimal designs accommodating larger bias voltages.

4. DISCUSSION AND CONCLUSION

In summary, we have demonstrated electro-optomechanical transduction from microwave photons to telecom-band optical photons via gigahertz-frequency mechanical modes. Our experiment takes advantage of the electrostatic force in a DC-biased capacitor as a mechanism for actuating gigahertz-frequency mechanical vibrations in a phononic crystal resonator, and routing mechanical waves through a phononic waveguide to an optomechanical cavity. Fabricating devices based on this concept, we show microwave-optical frequency conversion with a photon conversion efficiency reaching $1.72 \pm 0.14 \times 10^{-7}$ at a bandwidth exceeding 3 MHz, and efficient phase modulation with a half-wave voltage of $V_\pi = 750$ mV, comparable to the counterparts with piezoelectric materials (see Supplement 1). Our devices are made from a conventional silicon-on-insulator platform, operate at room temperature and atmosphere pressure, and do not rely on intrinsic material properties such piezoelectricity or the Pockels effect, therefore offering a universal mechanism adoptable to wide range of material platforms. Looking ahead, we anticipate several orders of magnitude improvement in the transduction efficiency with operation

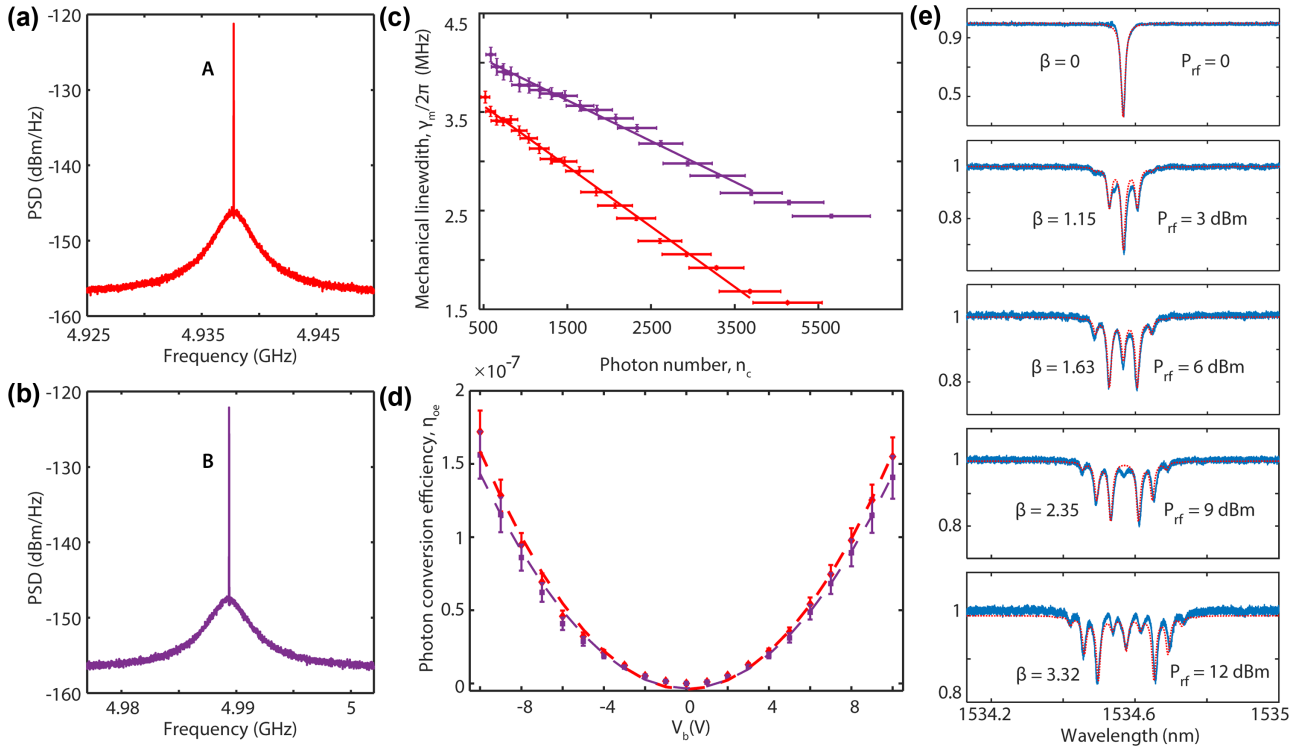

Fig. 4. Calibrating microwave-optics conversion efficiency. (a) Power spectral density (PSD), showing the driven response (the narrow central peak) and the thermal Brownian motion (the broad baseline feature) for the mechanical mode A. The microwave power is set to −40 dBm, and the DC-bias voltage is 10 V. The number of phonons is found as $n^{A}_{phon} = 1116$. (b) PSD for the mechanical mode B with the same microwave power and bias voltage as part (a), leading to $n^{B}_{phon} = 1457$. (c) Measured linewidths of the mechanical mode A (red) and B (purple) as a function of intra-cavity photon number from the pump laser. The vertical error bars designate the 95% confidence interval from a Lorentzian fit to the mechanical spectrum. The horizontal error bars represent an estimated 10% uncertainty arising from connections and reconnections of fiber mating unions during the calibration of intracavity photon numbers. (d) Microwave-to-optical photon flux conversion efficiency η_{oe} for the modes A and B as a function of the DC bias voltage. Measurements are done with an optical power of 46 μW ($n_c = 980$) in the on-chip waveguide. The microwave drive power is kept sufficiently low (−6 dBm) to avoid high-order acousto-optic harmonic generation. The error bars are from analytical calculations and account for the uncertainties in calibrating the electromechanical decay and optomechanical coupling rates. (e) Optical reflection spectra for microwave drive tones result in a large modulation index. Red dotted curves are the theoretical fits from which we extract the modulation index (β). The DC bias voltage is set at 10 V for these measurements.

at milikelvin temperatures that will mark a significant step forward towards realizing efficient microwave-optical entanglement generations [39–41]. Gigahertz-frequency silicon mechanical oscillators exhibit exceptionally narrow spectral linewidths (in the 10–100 kHz range) at these temperatures [25–27], translating to significant improvements in the electromechanical and optomechanical cooperativities. Additionally, integration with high-impedance microwave cavities readily increases the electromechanical readout rate to previously demonstrated values in the range of 0.5–1 MHz [37]. With these parameters, we anticipate achieving efficiencies exceeding 50% at a bandwidth above 500 kHz using few μ-Watt optical pump powers, values at which continuous-wave operation has been demonstrated with NbTiN microwave resonators [39,42]. Our work may also open up new avenues for RF photonics applications such as filtering, isolation, frequency multiplication, and beam-steering [32–34] by enabling silicon devices compatible with the standard CMOS technology.

Funding. KNI-Wheatley Scholarship; California Institute of Technology, EAS Division; U.S. Department of Energy (1F-60579); Directorate for Engineering (2137645).

Acknowledgment. We acknowledge Peter Day at the NASA Jet Propulsion Laboratory for the deposition of TiN films.

Disclosures. The authors declare no conflicts of interest.

Data availability. All the data needed to evaluate the conclusions in the paper have been presented in the figures in the main text or the supplementary sections. Any additional data may be obtained from the authors upon reasonable request.

Supplemental document. See Supplement 1 for supporting content.

REFERENCES

1. X. Han, W. Fu, C.-L. Zou, L. Jiang, and H. X. Tang, "Microwave-optical quantum frequency conversion," Optica **8**, 1050–1064 (2021).
2. J. Holzgrafe, N. Sinclair, D. Zhu, A. Shams-Ansari, M. Colangelo, Y. Hu, M. Zhang, K. K. Berggren, and M. Lončar, "Cavity electro-optics in thin-film lithium niobate for efficient microwave-to-optical transduction," Optica **7**, 1714–1720 (2020).
3. T. P. McKenna, J. D. Witmer, R. N. Patel, W. Jiang, R. V. Laer, P. Arrangoiz-Arriola, E. A. Wollack, J. F. Herrmann, and A. H. Safavi-Naeini, "Cryogenic microwave-to-optical conversion using a triply resonant lithium-niobate-on-sapphire transducer," Optica **7**, 1737–1745 (2020).
4. Y. Xu, A. A. Sayem, L. Fan, C.-L. Zou, S. Wang, R. Cheng, W. Fu, L. Yang, M. Xu, and H. X. Tang, "Bidirectional interconversion of microwave and light with thin-film lithium niobate," Nat. Commun. **12**, 4453 (2021).
5. A. H. Safavi-Naeini, D. V. Thourhout, R. Baets, and R. V. Laer, "Controlling phonons and photons at the wavelength scale: integrated photonics meets integrated phononics," Optica **6**, 213–232 (2019).

6. L. Shao, M. Yu, S. Maity, N. Sinclair, L. Zheng, C. Chia, A. Shams-Ansari, C. Wang, M. Zhang, K. Lai, and M. Lončar, "Microwave-to-optical conversion using lithium niobate thin-film acoustic resonators," Optica **6**, 1498–1505 (2019).
7. W. Jiang, R. N. Patel, F. M. Mayor, T. P. McKenna, P. Arrangoiz-Arriola, C. J. Sarabalis, J. D. Witmer, R. V. Laer, and A. H. Safavi-Naeini, "Lithium niobate piezo-optomechanical crystals," Optica **6**, 845–853 (2019).
8. X. Han, W. Fu, C. Zhong, C.-L. Zou, Y. Xu, A. A. Sayem, M. Xu, S. Wang, R. Cheng, L. Jiang, and H. X. Tang, "Cavity piezo-mechanics for superconducting-nanophotonic quantum interface," Nat. Commun. **11**, 3237 (2020).
9. W. Jiang, C. J. Sarabalis, Y. D. Dahmani, R. N. Patel, F. M. Mayor, T. P. McKenna, R. Van Laer, and A. H. Safavi-Naeini, "Efficient bidirectional piezo-optomechanical transduction between microwave and optical frequency," Nat. Commun. **11**, 1166 (2020).
10. M. Forsch, R. Stockill, A. Wallucks, I. Marinković, C. Gärtner, R. A. Norte, F. van Otten, A. Fiore, K. Srinivasan, and S. Gröblacher, "Microwave-to-optics conversion using a mechanical oscillator in its quantum ground state," Nat. Phys. **16**, 69–74 (2020).
11. S. Hönl, Y. Popoff, D. Caimi, A. Beccari, T. J. Kippenberg, and P. Seidler, "Microwave-to-optical conversion with a gallium phosphide photonic crystal cavity," Nat. Commun. **13**, 2065 (2022).
12. R. Stockill, M. Forsch, F. Hijazi, G. Beaudoin, K. Pantzas, I. Sagnes, R. Braive, and S. Gröblacher, "Ultra-low-noise microwave to optics conversion in gallium phosphide," Nat. Commun. **13**, 6583 (2022).
13. J. Bochmann, A. Vainsencher, D. D. Awschalom, and A. N. Cleland, "Nanomechanical coupling between microwave and optical photons," Nat. Phys. **9**, 712–716 (2013).
14. H. Li, S. A. Tadesse, Q. Liu, and M. Li, "Nanophotonic cavity optomechanics with propagating acoustic waves at frequencies up to 12 GHz," Optica **2**, 826–831 (2015).
15. K. C. Balram, M. I. Davanço, B. R. Ilic, J.-H. Kyhm, J. D. Song, and K. Srinivasan, "Acousto-optic modulation and optoacoustic gating in piezo-optomechanical circuits," Phys. Rev. Appl **7**, 024008 (2017).
16. D. B. Sohn, S. Kim, and G. Bahl, "Time-reversal symmetry breaking with acoustic pumping of nanophotonic circuits," Nat. Photonics **12**, 91–97 (2018).
17. G. Bahl, J. Zehnpfennig, M. Tomes, and T. Carmon, "Stimulated optomechanical excitation of surface acoustic waves in a microdevice," Nat. Commun. **2**, 403 (2011).
18. A. Vainsencher, K. J. Satzinger, G. A. Peairs, and A. N. Cleland, "Bi-directional conversion between microwave and optical frequencies in a piezoelectric optomechanical device," Appl. Phys. Lett. **109**, 033107 (2016).
19. K. C. Balram, M. I. Davanço, J. D. Song, and K. Srinivasan, "Coherent coupling between radiofrequency, optical and acoustic waves in piezo-optomechanical circuits," Nat. Photonics **10**, 346–352 (2016).
20. R. V. Laer, W. Jiang, R. N. Patel, C. J. Sarabalis, A. Cleland, T. P. McKenna, E. A. Wollack, P. Arrangoiz-Arriola, J. D. Witmer, and A. H. Safavi-Naeini, "Piezo-optomechanics in lithium niobate on silicon-on-insulator for microwave-to-optics transduction," in *Conference on Lasers and Electro-Optics* (Optica, 2020), paper STu4J.2.
21. M. Mirhosseini, A. Sipahigil, M. Kalaee, and O. Painter, "Superconducting qubit to optical photon transduction," Nature **588**, 599–603 (2020).
22. I. Marinković, M. Drimmer, B. Hensen, and S. Gröblacher, "Hybrid integration of silicon photonic devices on lithium niobate for optomechanical wavelength conversion," Nano Lett. **21**, 529–535 (2021).
23. H. Zhao, B. Li, H. Li, and M. Li, "Enabling scalable optical computing in synthetic frequency dimension using integrated cavity acousto-optics," Nat. Commun. **13**, 5426 (2022).
24. J. Chan, A. H. Safavi-Naeini, J. T. Hill, S. Meenehan, and O. Painter, "Optimized optomechanical crystal cavity with acoustic radiation shield," Appl. Phys. Lett. **101**, 081115 (2012).
25. S. M. Meenehan, J. D. Cohen, S. Groeblacher, J. T. Hill, A. H. Safavi-Naeini, M. Aspelmeyer, and O. Painter, "Silicon optomechanical crystal resonator at millikelvin temperatures," Phys. Rev. A **90**, 011803 (2014).
26. G. S. MacCabe, H. Ren, J. Luo, J. D. Cohen, H. Zhou, A. Sipahigil, M. Mirhosseini, and O. Painter, "Nano-acoustic resonator with ultralong phonon lifetime," Science **370**, 840–843 (2020).
27. A. Wallucks, I. Marinković, B. Hensen, R. Stockill, and S. Gröblacher, "A quantum memory at telecom wavelengths," Nat. Phys. **16**, 772–777 (2020).
28. S. Sridaran and S. A. Bhave, "Electrostatic actuation of silicon optomechanical resonators," Opt. Express **19**, 9020–9026 (2011).
29. R. Van Laer, R. N. Patel, T. P. McKenna, J. D. Witmer, and A. H. Safavi-Naeini, "Electrical driving of X-band mechanical waves in a silicon photonic circuit," APL Photon. **3**, 086102 (2018).
30. M. Kalaee, M. Mirhosseini, P. B. Dieterle, M. Peruzzo, J. M. Fink, and O. Painter, "Quantum electromechanics of a hypersonic crystal," Nat. Nanotechnol. **14**, 334–339 (2019).
31. G. Arnold, M. Wulf, S. Barzanjeh, E. S. Redchenko, A. Rueda, W. J. Hease, F. Hassani, and J. M. Fink, "Converting microwave and telecom photons with a silicon photonic nanomechanical interface," Nat. Commun. **11**, 4460 (2020).
32. H. Tian, J. Liu, A. Siddharth, R. N. Wang, T. Blésin, J. He, T. J. Kippenberg, and S. A. Bhave, "Magnetic-free silicon nitride integrated optical isolator," Nat. Photonics **15**, 828–836 (2021).
33. L. Fan, C.-L. Zou, N. Zhu, and H. X. Tang, "Spectrotemporal shaping of itinerant photons via distributed nanomechanics," Nat. Photonics **13**, 323–327 (2019).
34. H. Li, Q. Liu, and M. Li, "Electromechanical brillouin scattering in integrated planar photonics," APL Photon. **4**, 080802 (2019).
35. G. M. Rebeiz, *RF MEMS: Theory, Design, and Technology* (Wiley, 2004).
36. M. Poot and H. X. Tang, "Broadband nanoelectromechanical phase shifting of light on a chip," Appl. Phys. Lett. **104**, 061101 (2014).
37. A. Bozkurt, H. Zhao, C. Joshi, H. G. LeDuc, P. K. Day, and M. Mirhosseini, "A quantum electromechanical interface for long-lived phonons," arXiv, 2207.10972 (2022).
38. M. J. Burek, C. Meuwly, R. E. Evans, M. K. Bhaskar, A. Sipahigil, S. Meesala, B. Machielse, D. D. Sukachev, C. T. Nguyen, J. L. Pacheco, E. Bielejec, M. D. Lukin, and M. Lončar, "Fiber-coupled diamond quantum nanophotonic interface," Phys. Rev. Appl. **8**, 024026 (2017).
39. W. Jiang, F. M. Mayor, S. Malik, R. V. Laer, T. P. McKenna, R. N. Patel, J. D. Witmer, and A. H. Safavi-Naeini, "Optically heralded microwave photons," arXiv, 2210.10739 (2022).
40. R. Sahu, L. Qiu, W. Hease, G. Arnold, Y. Minoguchi, P. Rabl, and J. M. Fink, "Entangling microwaves with optical light," arXiv, 2301.03315 (2023).
41. S. Meesala, S. Wood, D. Lake, P. Chiappina, C. Zhong, A. D. Beyer, M. D. Shaw, L. Jiang, and O. Painter, "Non-classical microwave-optical photon pair generation with a chip-scale transducer," arXiv, 2303.17684 (2023).
42. B. M. Brubaker, J. M. Kindem, M. D. Urmey, S. Mittal, R. D. Delaney, P. S. Burns, M. R. Vissers, K. W. Lehnert, and C. A. Regal, "Optomechanical ground-state cooling in a continuous and efficient electro-optic transducer," Phys. Rev. X **12**, 021062 (2022).